A Distributed Architecture Based on Microbank Modules With Self-Reconfiguration Control to Improve the Energy Efficiency in the Battery Energy Storage System

Zhiliang Zhang, *Senior Member, IEEE*, Yong-Yong Cai, *Student Member, IEEE*, Yue Zhang, Dong-Jie Gu, and Yan-Fei Liu, *Fellow, IEEE*

***Abstract*—This paper proposes a new distributed battery energy architecture based on the microbank module (MBM) for dc microgrids. The benefits of the proposed architecture include: 1) no voltage sharing problem and no overcharge/overdischarge problem; 2) high compatibility and reliability; 3) high energy utilization efficiency; 4) reduced volume and weight of the battery management system (BMS). The proposed MBM consists of a microbidirectional dc/dc converter, a micro-BMS and a cell bank. Moreover, taking advantage of the battery recovery effect, a self-reconfiguration discharge strategy is also proposed to further enhance the battery performance and discharge efficiency of the new battery energy storage system (BESS). To optimize the proposed control, an efficiency analytical model considering the battery recovery effect is proposed using the curve fitting method. Owing to the bidirectional capability, soft switching capability and high efficiency, the dual active bridge (DAB) converters are chosen as the microbidirectional dc/dc converters. A hybrid modulation strategy with variable switching frequency combining the conventional phase-shift modulation and triangular current modulation is proposed for the DAB converter to reduce the dominant loss and improve the efficiency in wide load range based on the minimum loss model. A 1.5-kW experimental testing platform consisting of four MBMs and four 12 V/100 Ah lithium battery modules was built to verify the proposed architecture with the control and the proposed model. The experimental results show that the discharge time of the proposed distributed BESS is increased significantly under wide operation condition with the self-reconfiguration control. The discharge efficiency of the BESS is improved by 7.1% with the idling time of 5 min under the power level of 1.5 kW.**

***Index Terms*—Battery energy storage system (BESS), battery management system (BMS), battery recovery effect, dual active bridge (DAB), self-reconfiguration, zero voltage switching (ZVS).**

Manuscript received October 5, 2014; revised December 14, 2014; accepted February 11, 2015. Date of publication February 24, 2015; date of current version September 21, 2015. This work was supported by the Fundamental Research Funds for the Central Universities (NUAA), NE2014101. Recommended for publication by Associate Editor B. Semail.

Z. Zhang, Y.-Y. Cai, Y. Zhang, and D.-J. Gu are with the Jiangsu Key Laboratory of New Energy Generation and Power Conversion, Nanjing University of Aeronautics and Astronautics, Nanjing 210016, China (e-mail: zlzhang@nuaa.edu.cn; cyy@nuaa.edu.cn; yuezhang@nuaa.edu.cn; dongjiegu@nuaa.edu.cn).

Y.-F. Liu is with the Department of Electrical and Computer Engineering, Queen's University, Kingston, ON K7L 3N6 Canada (e-mail: yanfei.liu@queensu.ca).

Color versions of one or more of the figures in this paper are available online at http://ieeexplore.ieee.org.

Digital Object Identifier 10.1109/TPEL.2015.2406773

ACRONYMS

ACMG	Ac microgrid.
BESS	Battery energy storage system.
BMS	Battery management system.
CPM	Conventional phase-shift modulation.
DAB	Dual active bridge.
DCMG	Dc microgrid.
DHB	Dual half bridge.
DPS	Dual phase shift.
EPS	Extended phase shift.
FB	Full bridge.
SMES	Superconducting magnetic energy storage.
SOC	State of charge.
TCM	Triangular current modulation.
VSF	Variable switching frequency.
ZCS	Zero current switching.
ZVS	Zero voltage switching.

I. INTRODUCTION

WITH the development of society, the power demand is increasing rapidly, as well as the scale of power grid. However, the large scale power grid has the following disadvantages, such as high cost, difficult to operate and low reliability. Nowadays, with the fast improvement of the power electronics, the power system tends to be microminiaturized and distributed, which gives rise to a novel conception, "MicroGrid" [1]. The MicroGrid can achieve the distributed power generation effectively and consists of the distributed energy sources and loads according to a certain topologic structure. Currently, the MicroGrid has two main forms, ac MicroGrid (ACMG) and dc MicroGrid (DCMG). Though the ACMG is used more widely by far, the DCMG have the following advantages: 1) low cost and loss; 2) high power factor; 3) it can transmit more energy than the ACMG under the same condition [2], [3]. As a result, the DCMG has become an interesting research topic recently.

Fig. 1 shows the MicroGrid in future home based on a dc bus. The energy storage unit is a critical part of the MicroGrid. It not only guarantees the stability, but also increases the energy efficiency of the system [4], [5]. The energy storage devices mainly include the battery, the supercapacitor, the high-speed flywheel and the superconducting magnetic energy storage, etc.

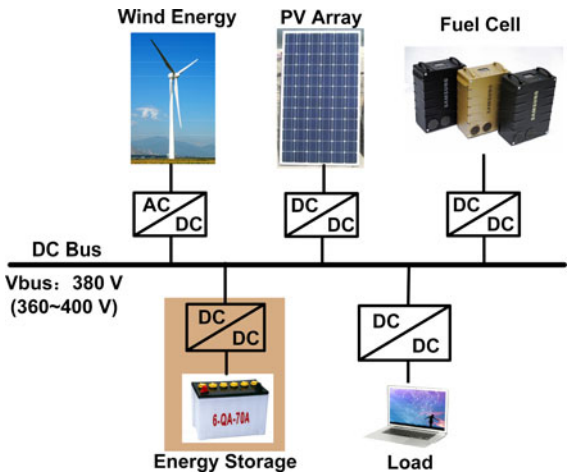

Fig. 1. Microgrid based on dc bus.

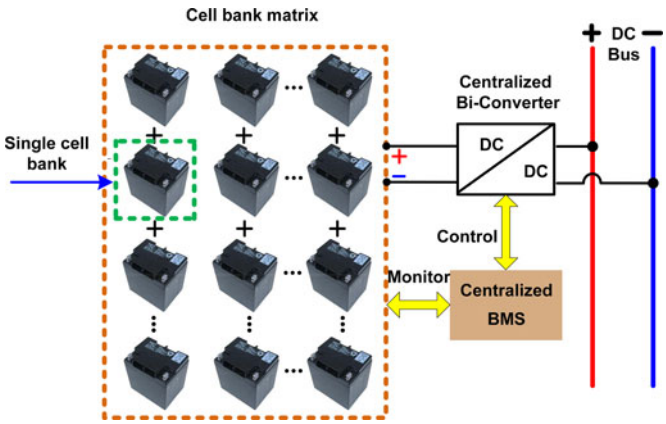

Fig. 2. Conventional centralized BESS.

The storage battery attains a promising application due to the advantages of high power density, flexibility and so on.

Fig. 2 shows the conventional centralized battery energy storage system (BESS). Normally, multiple cell banks build a storage unit in a matrix. The unit feeds the dc bus via a centralized bidirectional dc/dc converter. A centralized battery management system (BMS) is used to control the energy flow. The BMS controls the power flow of the converter by monitoring the voltage, temperature and state of charge (SOC) of each cell bank. Though the centralized BESS is widely used by now, it still suffers the flowing drawbacks: 1) voltage sharing and over charge/discharge problem; 2) low efficiency and reliability; 3) low flexibility; 4) poor compatibility; and 5) high production cost, etc.

From Fig. 2, it is noted that the bidirectional dc/dc converter plays an important role in the BESS. In high voltage applications, different transformer-based bidirectional converters were proposed such as the full bridge converter [6], the dual active bridge (DAB) converter [7], the dual half bridge converter [8] and the resonant converter topologies [9]. Among these topologies, the DAB converter as shown in Fig. 3 is widely used in the BESS owing to the electrical isolation, high reliability and soft switching capability [10]. The leakage inductance of the

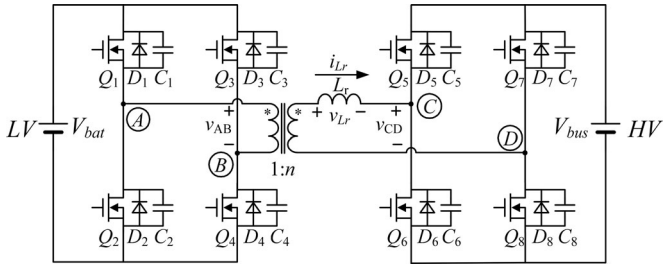

Fig. 3. DAB converter in the battery application.

transformer can also be absorbed by the resonant inductance. Normally, the conventional phase-shift modulation (CPM) was applied to the DAB converters [11]. The benefit is the soft switching capability to minimize the switching loss in the DAB converters. However, the range of the soft switching is limited depending on the voltage conversion ratio and on the load current [12], [13].

To extend the ZVS range of the DAB converters, an extended phase shift control was proposed by modulating the duty cycle of either the primary side or the secondary side voltage [14]. The dual phase shift control methods were proposed in order to reduce the inductor RMS current or to extend ZVS range further [15]. Among the control strategies, the triangular current modulation (TCM) attracts more interest to improve the light load efficiency due to lower inductor current and zero current switching (ZCS) characteristic [16].

The contribution of this paper is to propose a new distributed structure of BESS to solve the problem exists in the centralized BESS. Moreover, a self-reconfiguration control strategy is proposed to further improve the discharge efficiency based on the battery recovery effect in the BESS. In order to achieve a high efficiency in wide range load, a variable switching frequency (VSF) hybrid control is proposed for the DAB converter. Under light load condition, the TCM with VSF is applied to minimize the total loss. Different from the approaches previously proposed in the literature, the VSF hybrid control in this paper is based on the overall loss optimization directly other than reduction of the reactive power or RMS current, which is more effective in the perspective of improving the efficiency in wide load range.

Section II presents the proposed distributed structure of BESS and its advantages. Section III presents the proposed self-reconfiguration control strategy. Section IV presents the proposed VSF hybrid control strategy and the loss analysis of the TCM. Section V demonstrates the simulation results. The experimental results and discussion are given in Section VI. Section VII provides a brief conclusion.

II. Proposed Distributed BESS Based on Microbank Modules (MBMs)

A. Proposed Architecture Based on MBMs

Fig. 4(a) shows the basic block diagram of an MBM. The basic MBM consists of a microbidirectional dc/dc converter, a micro-BMS and a cell bank. In order to optimize the characteristics

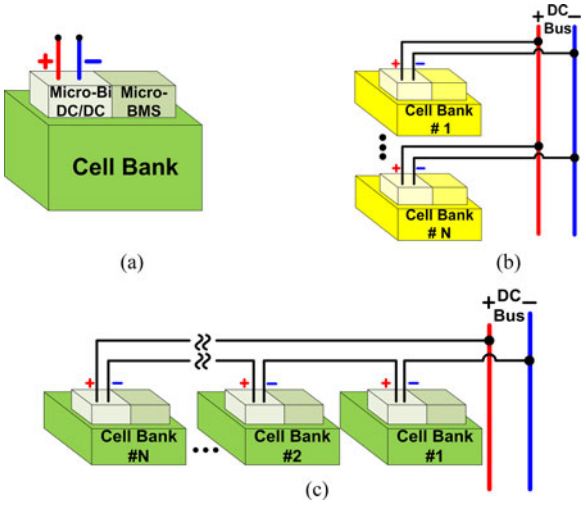

Fig. 4. Proposed MBM and configuration architecture.

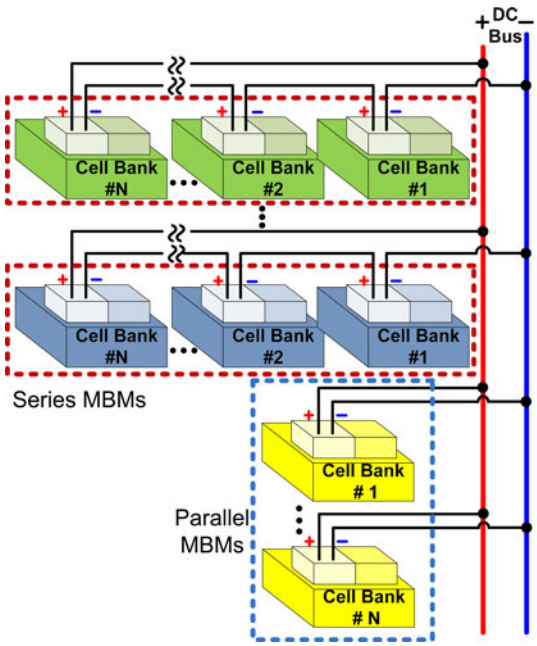

Fig. 5. Proposed architecture based on the MBMs for BESS.

of the single cell bank, the MBM is controlled independently according to its optimal charge and discharge curve. The MBMs can also be combined in series or parallel in order to meet different current and voltage requirement. Fig. 4(b) and (c) gives the parallel and series configuration, respectively. Moreover, the series array and parallel array of the MBMs can be combined together as shown in Fig. 5. This leads to great flexibility of the constructed architecture.

Fig. 6 shows the hybrid BMS of the centralized BMS and distributed micro-BMS. The micro-BMS in each MBM is connected to a centralized BMS via the CAN bus to form a hierarchic structure of the BMS. This will drastically reduce the size and weight of the conventional centralized BMS. Meanwhile, it

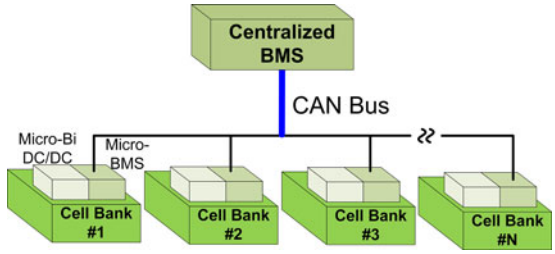

Fig. 6. Hybrid BMS of the centralize BMS and distributed micro-BMS.

can avoid a large wiring harness, and provides a large reduction in the number of the modules and the cost.

B. Benefits of Proposed Architecture

Compared with the centralized BESS, the proposed architecture has the following advantages:

1) *No Voltage Sharing and Overcharge/Overdischarge Problem:* In the proposed architecture, each cell bank is integrated with a Micro-Bi dc/dc converter and a Micro-BMS. Hence, the voltage and current of each cell bank are managed independently. This solves the voltage sharing problem as well as the overcharge/overdischarge problem. Moreover, this enables the cell bank to operate under the optimal control and improve the efficiency and performance.
2) *High Compatibility:* The MBMs function as an interface between different types of cell banks and the dc bus. This allows various types of cell banks to coexist in the proposed architecture as long as they produce the required voltage and current via the MBMs, so that the compatibility is increased greatly.
3) *High Reliability With the Decoupling Control of Each MBM:* The MBM allows the decoupling control and removes the possible negative influence on the cell banks when the fault happens. As a result, the proposed system has high tolerance to the faults and high reliability compared with the conventional centralized BESS.
4) *Better Space Utilization:* In the centralized BESS, the cell banks are placed around and a large space is needed. This leads to the low utilization efficiency of space. However, for the proposed architecture, an MBM owns low profile and high convenience to plug in. The MBMs can be integrated into the MicroGrid more conveniently and efficiently, which improves the space utilization efficiency.
5) *Hybrid Combination Capability of Centralize BMS and Distributed BMS for Low Profile and Cost:* Due to the module structure of the MBM, the micro-BMS can be combined with the centralized BMS to form a hierarchic structure of the BMS. This will drastically reduce the size and weight of the conventional centralized BMS. At the same time, it can avoid a large wiring harness, and provide a large reduction in the number of modules and the cost.

III. Proposed Self-Reconfiguration Control Based on Battery Recovery Effect

A. Battery Recovery Effect

There are varieties of energy optimization studies in the literature that mostly consider batteries as ideal energy reservoirs. However, most commercial batteries are governed by the complex nonlinear internal chemical reactions to provide energy [17], [18]. It is interesting to note that when the battery idles during some period without discharging, the diffusion process compensates for the depletion of the active materials during discharge and battery output voltage increases [19]. This phenomenon has been observed in various types of batteries, such as lead-acid battery, lithium battery, Ni-Cd battery, etc. That is the nonlinear discharge characteristic obtained by most batteries—the recovery effect, that is, the deliverable energy in a battery can be self-replenished, if left idling for sufficient time.

B. Proposed Self-Reconfiguration Control Strategy

The battery recovery effect opens up the possibility of the battery scheduling in the multiple-battery systems. The controlled switch matrix is used to reconfigure the composite structure of multiple cell banks automatically according to the dynamic load/storage demand in [20] and [21]. There exist two types of the battery discharge mode. The first one is the continuous discharge without any relaxation (period of rest). The second one is the intermittent discharge, which implies that the battery goes through periods of rest between successive discharge. In the centralized BESS, each battery bank discharges simultaneously and can only apply the continuous discharge mode without the recovery time. But in the proposed architecture, the battery banks are controlled by the local micro dc/dc converters independently. So the self-reconfiguration strategy is proposed to increase the energy utilization of the BESS. The main idea here is to use multiple batteries in an intermittent discharge fashion to prolong the discharge time of the battery storage system. The operation condition of each battery is depended on its SOC. In each discharge cycle, the battery with the lowest SOC idles to recover capacity while others are still active to supply the energy.

Fig. 7 shows the block diagram of the proposed control. Based on the information of the battery bank, etc., the voltage, current, the micro-BMS can estimate the SOC of each battery bank from (1)

$$\mathrm{SOC}_t = \mathrm{SOC}_0 - \frac{1}{C_N}\int_0^t i(\tau)\,d\tau \tag{1}$$

where SOC_0 is the initial SOC and is determined by the open-circuit voltage of the battery bank, $i(\tau)$ is the discharge current and C_N is the rated capacity. The method presented by (1) is called "Coulomb Counting Method." Compared with other SOC estimation methods, this method is normally applied to estimate the SOC and more accurate when the battery is discharging.

Seen from Fig. 7, with the optimal scheduling algorithm of the self-reconfiguration discharge strategy, the SOC of each battery bank is calculated real time. Then, the SOC information of each bank is shared by the micro-BMS. The obtained PWM control signals communicate between the local micro-BMS and dc/dc converter. The optimal scheduling algorithm is shown in Fig. 8. Initially, the range of the operation SOC is set. First, the banks that meet the range of the operation SOC are determined and sorted in a descending order in terms of their average SOC. Then, the first ranking *N* banks are selected to discharge depending on the load requirement. This reconfiguration can be performed with a constant time interval *T*. The key point of the proposed self-reconfiguration control is based on the battery recovery

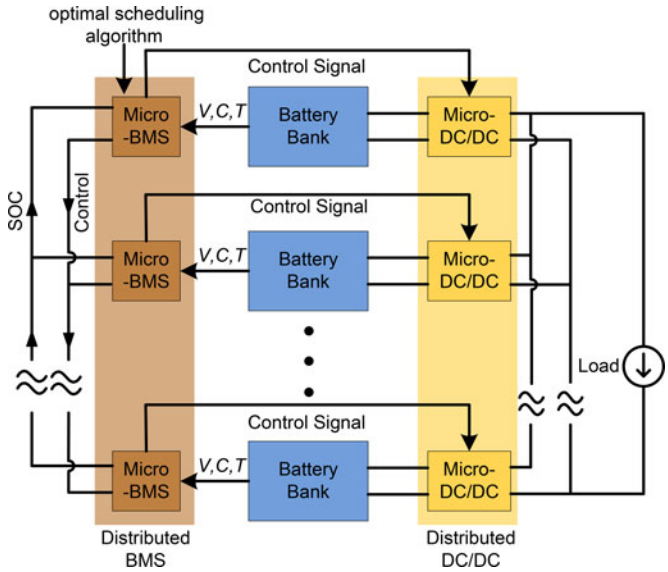

Fig. 7. Block diagram of proposed self-reconfiguration control.

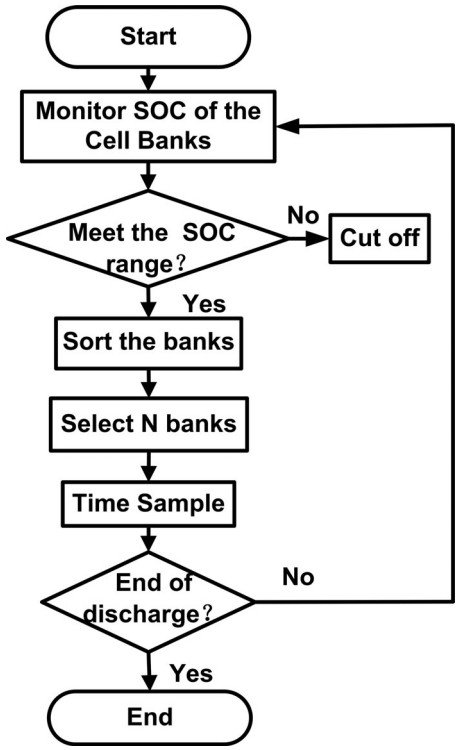

Fig. 8. Flow chat of proposed algorithm.

effect, the battery with the lowest SOC idles to take the recovery process, so the energy efficiency of the distributed BESS system could be improved significantly.

Actually, if the load is heavy, the self-reconfiguration discharge strategy will not be applied and all batteries are active and provide energy to the load at the same time. Therefore, the maximum output power of the distributed BESS with the self-reconfiguration control is the same as the maximum output power with respect to the one without the self-reconfiguration control.

C. Modeling of Energy Improvement Efficiency Based on the Battery Recovery Effect

It is noted that the proposed self-reconfiguration control strategy is based on the battery recovery effect. The energy efficiency improvement with the proposed control depends on the discharge current and idling time of the batteries. Therefore, an efficiency model considering the recovery effect is helpful to predict the energy utilization of the batteries quantitatively and maximum the overall performance of the BESS. Actually, there is a design tradeoff between the idling time and discharge current to maximize the efficiency of the proposed control.

There is a wide variety of the battery modeling methods, which can capture battery behavior for specific purposes. The electrochemical battery models in [22]–[24] describe the fundamental mechanisms of the battery design process and are used to optimize the physical design aspects of batteries. The electrical battery models in [25]–[28] are the electrical equivalent model using a combination of the voltage sources, resistors and capacitors to capture the *I*–*V* characteristics of batteries. The hybrid battery models in [29] and [30], which are based on the electrical battery model and kinetic battery model, can capture the dynamic characteristics and nonlinear behaviors of the batteries more accurately. Some of these models have mentioned the battery recovery effect. However, none of these models has a specific and intuitive description of the recovery effect in the modeling of the battery. Therefore, using the aforementioned models in the simulation of the conventional BESS, the advantage of the recovery effect could not be demonstrated and predicted precisely.

The idea proposed here is to use the curve fitting method to build the efficiency model of the recovery effect based on the measured discharge curves of the batteries when the reconfiguration control is applied. Normally, the recovery curve can be obtained based on the measurement of the batteries. As an example, Fig. 9(a) shows the characteristic curve of the battery recovery effect. From Fig. 9(a), when the battery is discharged with the discharge current of $i_{\rm dis}$, the battery voltage reduces continuously. At t_1, the battery stops discharging, and the battery voltage starts to recover and increase during the idling time. As the blue curve shown in Fig. 9(a), the recovery curve is steep initially and tends to become smooth as the idling time increases. Basically, the battery recovery effect is influenced by three factors including the active time tact, the idling time $t_{\rm idl}$ and the discharge current $i_{\rm dis}$. On the other hand, the battery open-circuit voltage (OCV) is related to the SOC. Actually, the SOC is a function of the battery OCV. This SOC estimation method is called the "OCV Method." During the relaxation phases, there is no discharging current, so (1) is not applicable to estimate the SOC. Therefore, the OCV method is used to estimate the SOC when the battery is idling to take the recovery effect. On the other hand, compared with other SOC estimation methods, the OCV method is more accurate with the idling battery. Fig. 9(b) shows the typical curve between the OCV and SOC of the iron phosphate Li-ion battery. It is noted that the recovered SOC is a function of the recovered voltage.

Combining Fig. 9(a) and (b), the transfer function between the recovered SOC and idling time is derived as shown in Fig. 9(c). Fig. 9(c) shows the curve of the recovered SOC versus the idling time. Using the curve fitting method, the recovered SOC curve as the function of the idling time $t_{\rm idl}$ can be expressed as analytically

$$\mathrm{SOC}_{\rm rec}(t_{\rm idl}, t_{\rm act}, i_{\rm dis}) = a \cdot \arctan(t_{\rm idl}^{b}) \cdot \arctan\left(t_{\rm act}^{c}\right) \cdot i_{\rm dis}^{\rm d} \tag{2}$$

where $t_{\rm idl}$ is the idling time, $t_{\rm act}$ is the active time, $i_{\rm dis}$ is the discharge current, and *a*, *b*, *c* and *d* are the correction factors, depending on the different battery measured recovery curves.

In the proposed architecture, the recovered energy for each idling cycle $Q_{r\text{-cycle}}$ can be expressed as

$$Q_{r\text{-cycle}} = \mathrm{SOC}_{\rm rec} \cdot Q_{\,\rm mod} \tag{3}$$

where $Q_{\rm mod}$ is the capacity of each battery module and $\mathrm{SOC}_{\rm rec}$ is the recovered SOC.

From (3), the recovered energy for each module Q_r is

$$Q_r = N \cdot Q_{r\text{-cycle}} = N \cdot \mathrm{SOC}_{\rm rec} \cdot Q_{\,\rm mod} \tag{4}$$

where *N* is the number of the idling cycle times of each battery module.

From (4), the total active time of each battery module $t_{\rm totoal}$ is

$$t_{\rm total} = \frac{Q_{\,\rm mod} + Q_r}{i_{\rm dis}} = \frac{Q_{\,\rm mod} + N \cdot \mathrm{SOC}_{\rm rec} \cdot Q_{\,\rm mod}}{i_{\rm dis}} \tag{5}$$

where $i_{\rm dis}$ is the discharge current.

In order to guarantee that each module is involved in the discharge process, the active time $t_{\rm act}$ and the idling time $t_{\rm idl}$ of the battery module has the following relationship:

$$t_{\rm act} = \frac{M'}{M - M'} \cdot t_{\rm idl} \tag{6}$$

where *M* is the total number of the battery modules, and *M′ is* the number of the active battery modules.

The number of the idling cycle times of each battery module *N* is

$$N = \frac{t_{\rm total}}{t_{\rm act}} \tag{7}$$

where $t_{\rm total}$ is the total active time of each battery module and $t_{\rm act}$ is the active time in each cycle.

Substituting (5) and (6) into (7), *N* can be expressed as

$$N = \frac{Q_{\,\rm mod}}{\frac{i_{\rm dis} \cdot M'}{M - M'} \cdot t_{\rm idl} - \mathrm{SOC}_{\rm rec} \cdot Q_{\,\rm mod}}. \tag{8}$$

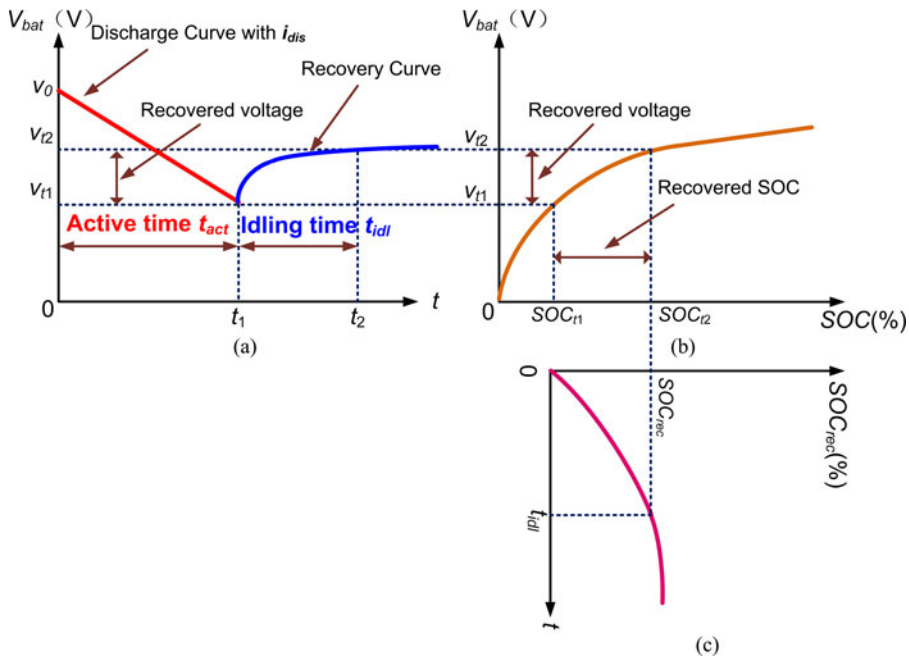

Fig. 9. (a) Characteristic curve of the battery recovery effect. (b) Typical curve between the OCV and SOC of iron phosphate Li-ion battery. (c) Derived curve of the recovered SOC versus the idling time.

The recovered energy for the system $Q_{r\text{-total}}$ is

$$Q_{r\text{-total}} = M \cdot Q_r \tag{9}$$

where Q_r is the recovered energy for each module and M is the total number of the battery modules.

The total energy of the system is

$$Q_{\text{total}} = M \cdot Q_{\text{mod}} \tag{10}$$

where Q_{mod} is the capacity of each battery module.

The efficiency of the recovered energy is defined as

$$\eta = \frac{Q_{r\text{-total}}}{Q_{\text{total}}}. \tag{11}$$

Substituting (9) and (10) into (11), combining (4), η can be derived as

$$\eta = \frac{Q_r}{Q_{\text{mod}}} = N \cdot \text{SOC}_{\text{rec}}. \tag{12}$$

Substituting (2) and (8) into (12), combining (6), η can be expressed as

As a result, (13), as shown at the bottom of the page, is the analytical model of the energy improvement efficiency η, where a, b, c, and d can be obtained by the curve fitting method on the recovery effect, M, M', Q_{mod}, t_{act}, t_{idl} and i_{dis} are determined by the design requirement of the BESS.

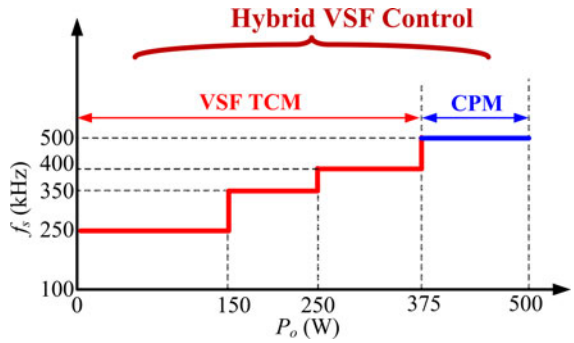

Fig. 10. Proposed VSF hybrid control.

IV. Proposed VSF Hybrid Control for DAB Converters

A. Proposed VSF Hybrid Control for DAB Converters

The DAB converters are chosen for the MBMs in the battery application. The battery voltage V_{bat} is 10.8∼13.8 V, the bus voltage V_{bus} is 360∼400 V and the turn ratio n is 16. Fig. 10 shows the proposed VSF hybrid control strategy. The VSF TCM is applied under light load condition to minimize the overall loss of the switching loss, the conduction loss, the drive loss and the copper loss of the transformer. On the one hand, the TCM can reduce the inductor RMS current for lower conduction loss due to the discontinuous current. On the other hand, with the TCM, six switches can achieve ZCS turn on and turn off, and the other two switches can achieve ZVS turn on for low

$$\eta = \frac{a \cdot \arctan(t_{\text{idl}}^b) \cdot \arctan\left[\left(\frac{M'}{M-M'} \cdot t_{\text{idl}}\right)^c\right] \cdot i_{\text{dis}}^d \cdot Q_{\text{mod}}}{\frac{i_{\text{dis}} \cdot M'}{M-M'} \cdot t_{\text{idl}} - a \cdot \arctan(t_{\text{idl}}^b) \cdot \arctan\left[\left(\frac{M'}{M-M'} \cdot t_{\text{idl}}\right)^c\right] \cdot i_{\text{dis}}^d \cdot Q_{\text{mod}}} \tag{13}$$

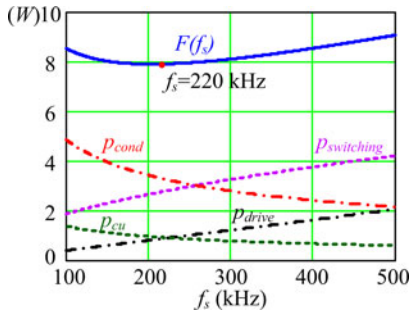

Fig. 11. Optimization curve with the conventional TCM: power loss versus switching frequency ($P_o = 150$ W).

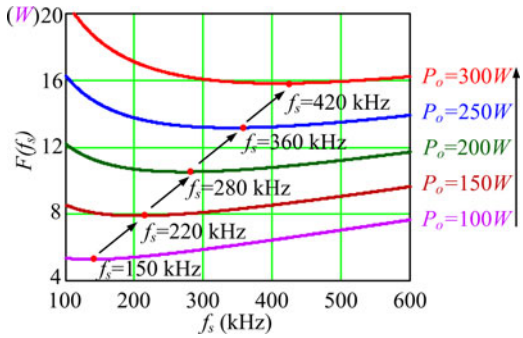

Fig. 12. Optimization curve with TCM under different load condition: power loss versus switching frequency.

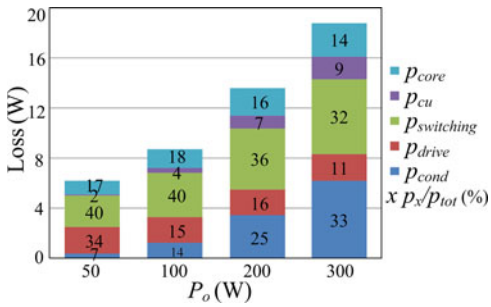

Fig. 13. Loss distribution of DAB converter with conventional TCM: $f_s = 500$ kHz.

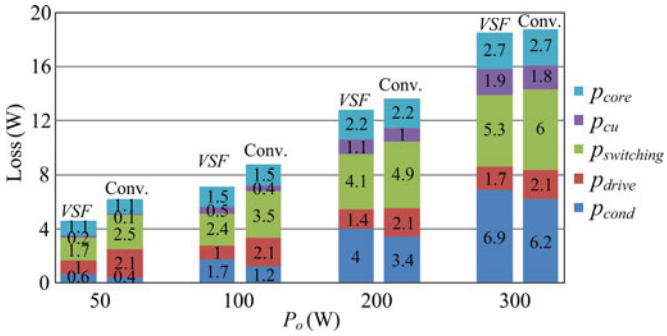

Fig. 14. Loss distribution comparison between proposed VSF and conventional TCM.

switching loss. When the output power exceeds the TCM power transfer threshold under heavy load condition, the CPM with the constant switching frequency is applied. With the CPM under heavy load condition, all switches can achieve ZVS turn on and high efficiency can be achieved. With the combination of the CPM and TCM, the advantages of the CPM and TCM are taken to achieve high efficiency during wide load range. In this case, the maximum power transferred with the TCM under the switching frequency of 400 kHz is 380 W, so 375 W is chosen as the boundary of CPM and TCM.

Compared to the conventional CSF TCM proposed previously, the key of the proposed VSF TCM is to find the optimal switching frequency to minimize the overall loss. With the TCM, lower switching frequency normally leads to higher inductor RMS current due to the increase of the peak inductor current. High switching frequency is desired to reduce the conduction loss when the output power increases. Nevertheless, high switching frequency also results in high switching loss and gate drive loss. This leads to a design tradeoff to select the optimal switching frequency between the conduction loss, switching loss and drive loss. However, the DAB converter with the conventional CSF TCM could not optimize the overall loss in wide load range.

Based on the analysis, Fig. 11 illustrates the optimal curve $F(f_s)$ with the TCM as a function of switching frequency f_s

$$F(f_s) = p_{\text{switching}} + p_{\text{drive}} + p_{\text{cond}} + p_{cu} \tag{14}$$

where $p_{\text{switching}}$ is the switching loss, p_{drive} is the drive loss, p_{cond} is the conduction loss of MOSFETs, and P_{cu} is the copper loss of the transformer. It should be noted that for the high frequency transformer, when the excitation frequency f goes up, the peak flux density B is reduced by the same amount; on the other hand, the loss coefficients α, β of the selected material in this paper are quite similar, the core losses remain essentially unchanged with variable operating frequency. Therefore, it is not included in (14) as the objective function.

It is observed that $F(f_s)$ is a U-shaped curve, and therefore, the optimization switching frequency under this condition can be located at the lowest loss point of the curve. Seen from Fig. 11, the optimal f_s can be chosen as 220 kHz in this case.

It should be noted that in Fig. 11, the optimal point is decided under the output power of 150 W. Actually, the optimal points depending on the total loss change when the output power varies. Fig. 12 gives the optimal curves under different load condition. It is observed that when the output power increases from 100 to 300 W, the optimal switching frequency varies from 150 to 420 kHz. This means that higher switching frequency leads to minimum total losses as the output power increases.

As shown in Fig. 12, the optimal VSF is desired to minimize the dominant loss with the TCM. It is interesting to notice that $F(f_s)$ varies little around the optimal point, which means there is no need to change the switching frequency with the load simultaneously.

It should be noted that the maximum switching frequency is limited by the core loss and skin effect of the magnetic. At the same time, the minimum switching frequency should also be limited to the saturation of the transformer core. Practically, the switching frequency is chosen from 250∼500 kHz according to the magnetic component in this application.

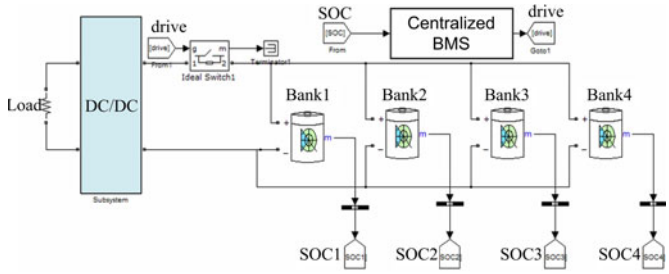

Fig. 15. Centralized BESS.

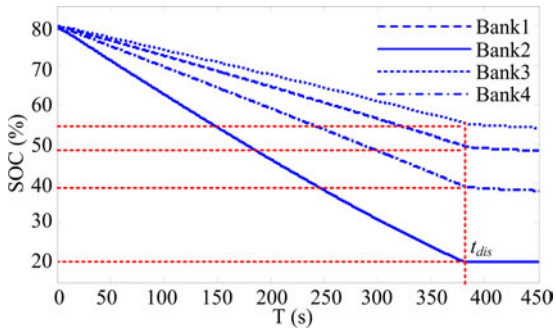

Fig. 16. SOC curves in BESS.

B. Loss Analysis and Comparison for the DAB Converter

1) Loss Analysis With Conventional TCM: Fig. 13 shows the loss distribution of the DAB converter with the conventional TCM under different load condition. It is noted that the dominant loss under 50 W condition are the drive loss $P_{\rm drive}$ and the switching loss $P_{\rm switching}$, which are 2.1 W (34%) and 2.5 W (40%), respectively. The dominant loss under 300 W condition are the conduction loss $P_{\rm cond}$ and $P_{\rm swithcing}$, which are 6.2 W (33%) and 6.0 W (32%), respectively. As the load condition increases, the percentage of $P_{\rm cond}$ increases and the percentage of $P_{\rm drive}$ decreases, respectively. $P_{\rm switching}$ takes a relatively high percentage during a wide load rang. Minimizing the dominant loss according to the load condition is an effective way to optimize the efficiency in wide load range.

2) Loss Distribution Comparison Between the Conventional CSF TCM and VSF TCM: Fig. 14 gives the loss distribution comparison of the DAB converter between the conventional CSF and the VSF with the TCM. One of the main design considerations is to optimize the size and volume of the magnetic components, and increase the power density. Therefore, the switching frequency of 500 kHz is chosen for the conventional CSF TCM to maintain the same power density and full load efficiency for fair comparison. As shown in Fig. 14, the total loss is reduced by 1.8 W under 50-W load condition, which translates into an efficiency improvement of 3.6%. It is noted the efficiency improvement is more effective under the light load condition. This is because under the light load condition, the drive loss and the switching loss become dominant loss among the total loss. The optimal switching frequency can reduce the drive loss and the switching loss more effectively. Thus, the target to minimize the total loss of the DAB converter is achieved and high efficiency can be achieved.

V. Simulation Results

Fig. 15 shows the simulated model of the centralized BESS. Four battery banks in parallel feed the load via a centralized bi-dc/dc converter. Different internal resistance of the battery models is set intentionally to model the disparity. The SOCs of each battery are monitored in real time and sent to the centralized BMS.

Fig. 16 shows the simulation results of the centralized BESS. When the SOC of bank 2 reaches the threshold, the other three battery banks also stop discharging. It is calculated that the energy utilization is as low as 66.7%.

Fig. 17 shows the model of the proposed architecture. It should be pointed that each battery bank is connected to the local microbi dc/dc converter individually. Fig. 18 shows the simulation results. It is observed that each battery is fully discharged according to the SOC status. The difference of the discharge rate among batteries caused by the internal resistance difference is eliminated. The energy capacity is fully utilized. There is no potential circulating current among the battery banks.

The proposed self-reconfiguration discharge control is simulated on the proposed system in Fig. 17. The recovery effect is included in the battery model. The optimal scheduling algorithm of the self-reconfiguration discharge strategy in Fig. 8 is programmed in Matlab. In this case, N is set to be 3, and T is 50 s. Fig. 19 shows the results. The battery with the lowest SOC will be shutdown to take the recovery process at the interval of T. Owing to the battery recovery effect, the distributed BESS gains an extra energy capacity of 3 Ah, which is 12.5% of the original storage energy. This leads to an increasement of the discharge time as much as 13.6%. In the large scale BESS of several or even dozens of kilowatts, the energy capacity improvement is considerable.

VI. Experimental Results and Discussion

In order to verify the proposed self-reconfiguration control, the hardware platform has been built. Fig. 20 shows the photo of the hardware platform. The system consists of four MBMs, which can provide a maximum power of 500 W, respectively. With the proposed control, three MBMs are always active while one is idling. The system can provide a maximum power of 1500 W. The lithium battery module of 12 V/100 Ah from Pylon Technologies is chosen as the battery bank, and four battery banks are utilized.

The ZVS DAB converter is used as the Micro-Bi dc–dc converter. The Freescale DSP MC56F8257 is used as the Micro-BMS to implement the proposed control strategy. The specifications are as follows: battery voltage: $V_{\rm bat} = 10.8 \sim 13.8$ V; bus voltage: $V_{\rm bus} = 360 \sim 400$ V; output power: $P_o = 500$ W; switching frequency: $f_s = 250 \sim 500$ kHz. The component of the power train are as follows: the transformer turns ratio: $n = 1{:}16$; total inductance $L_r = 30$ μH; LV side MOSFETs $Q_1 \sim Q_4$: BSC014N03LS (30 V/100 A/1.4 mΩ from Infineon); HV side MOSFETs $Q_5 \sim Q_8$: IPP65R380E6 (650 V/10.6 A/0.38 Ω from Infineon). A Hall-effect sensor BJHCS-PS25 is used to sample the LV side current and a

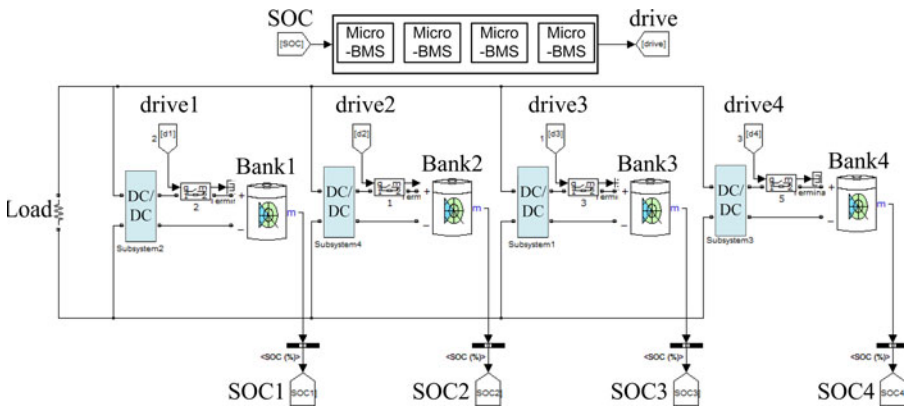

Fig. 17. Proposed distributed BESS.

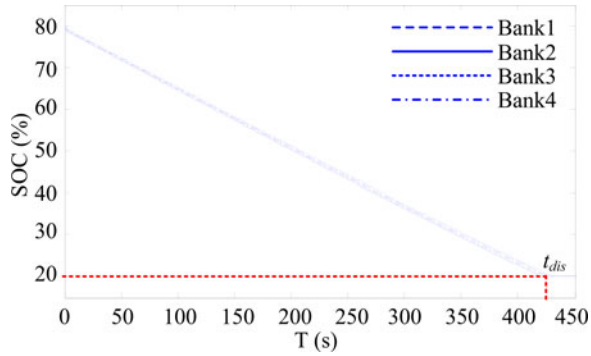

Fig. 18. SOC curves in the distributed system.

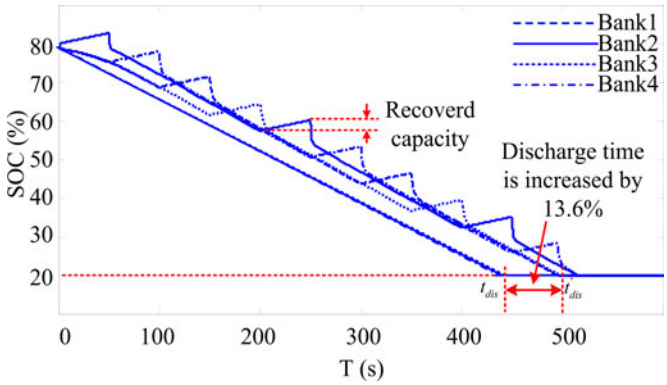

Fig. 19. SOC curves in the distributed BESS with self-reconfiguration discharge strategy.

Hall-effect-based linear current sensor IC ACS712ELCTR-05B-T is used to sense the HV side current. Two isolation amplifiers HCPL-7840 are used to sample the LV and HV side voltage, respectively.

A. *Verification of Proposed Self-Reconfiguration Control*

In order to do a fair comparison, two different experimental scenarios are set to verify the proposed self-reconfiguration control under variable conditions.

1) Same Idling Time With the Different Power Level: In the test, the distributed BESS consists of four MBMs. With the

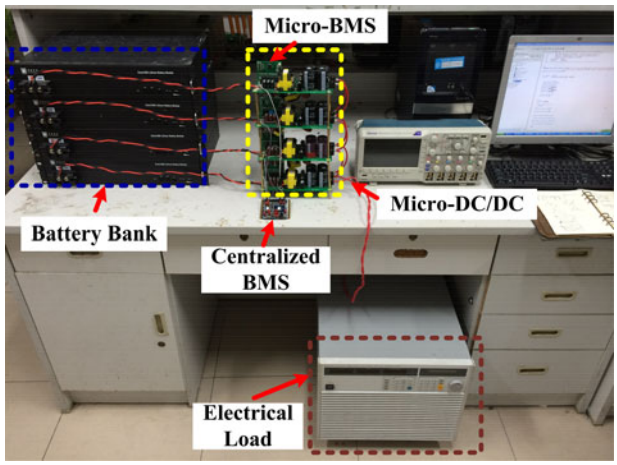

Fig. 20. Photo of experimental testing platform.

proposed self-reconfiguration control strategy, three MBMs are active to provide the output power while one stands by. In order to verify the proposed control strategy in a wide load range, the power level of the BESS is set to be 750, 900, 1200 and 1500 W, corresponding to half load, 60% load, 80% load and full load of each active MBM in the system with the proposed control. The idling time is 15 min.

Fig. 21(a) shows the discharge curves of the MBM with and without the proposed self-reconfiguration control in the distributed BESS under a power level of 1200 W. In the distributed BESS with the conventional control, all of the four MBMs are active, and each MBM provides 300 W. So the discharge time of the system is determined by the MBM which reaches the voltage threshold first, as the red curve shown in Fig. 21(a). The left four curves represent the discharge curve of the four MBMs in the distributed BESS with the proposed self-reconfiguration control. While with the proposed control, three MBMs need to be active all the time, so the discharge time of the system is determined when two MBMs reach the threshold voltage. Then, the improved discharge time can be calculated. The idling time is for the battery to take the recovery process. It is observed that the voltage of the battery increases during the idling time, which demonstrates that the capacity of the battery can be increased owing to the battery recovery effect. As a result, the discharge

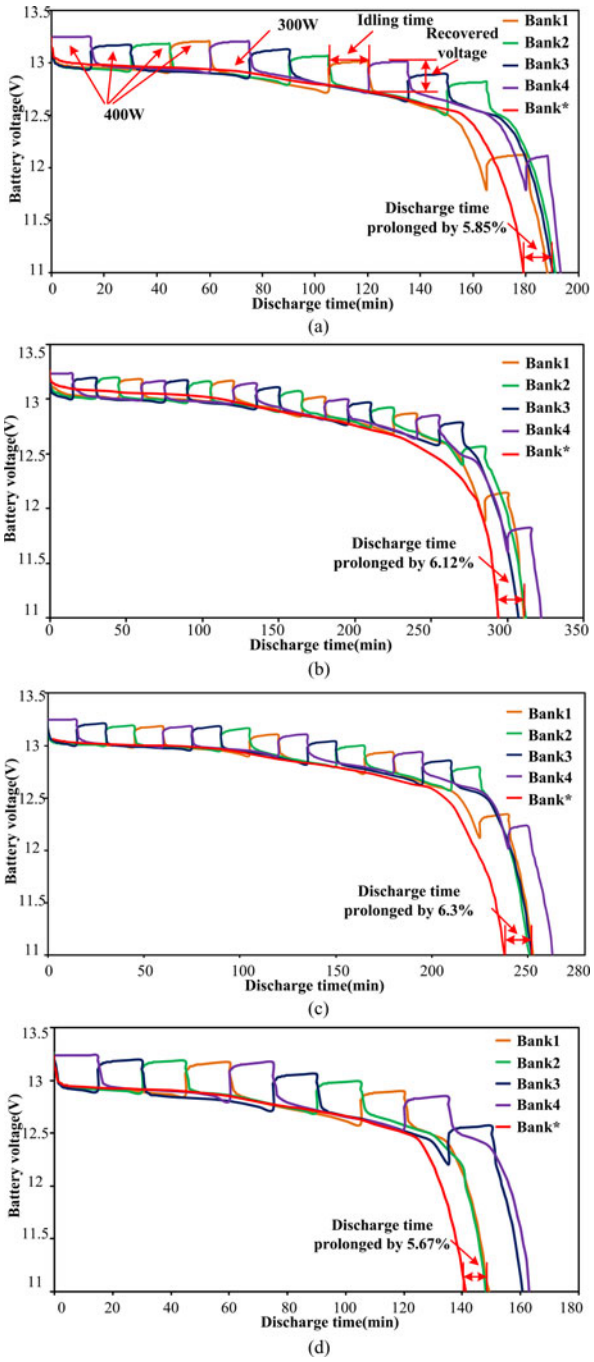

Fig. 21. Discharge curves of the MBM with different power level. (a) 1200 W; (b) 750 W; (c) 900 W; (d) 1500 W.

time of the BESS with the proposed control is extended by 5.85% under 1200 W. Fig. 21(b)–(d) shows the similar improvement with different power level of 750, 900 and 1500 W, respectively.

Table I summarizes the measured discharge time of the BESS with and without the proposed self-reconfiguration control. The discharge time of the BESS is increased by 6.12%, 6.3%, 5.85% and 5.67%, corresponding to the power level of 750, 900, 1200 and 1500 W.

TABLE I
MEASURED DISCHARGE TIME OF THE DISTRIBUTED BESS WITH THE IDLING TIME OF 15 MIN

Power level (W)	Conventional (min)	Proposed (min)	Improved efficiency
750	294	312	6.12%
900	238	253	6.3%
1200	179.5	190	5.85%
1500	141	149	5.67%

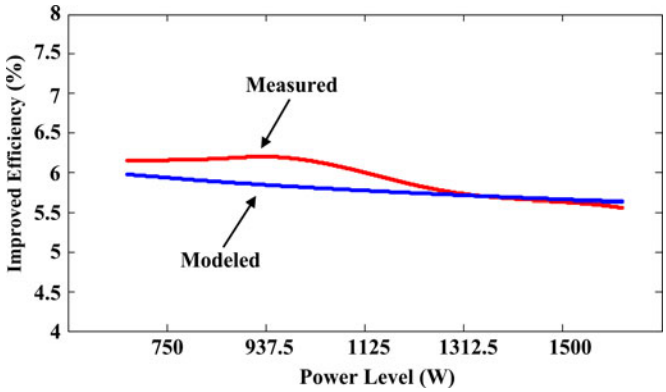

Fig. 22. Comparison of the measured and modeled energy improvement efficiency under different power level with the idling time of 15 min.

In the experimental testing platform, the BESS contains four battery modules, which are lithium battery modules of 12 V/100 Ah. Three battery modules are active all the time, and one is idling depending on the SOCs. Under this condition, the parameters in (13) have the following values, $Q_{\mathrm{mod}} = 100$, $M = 4$, and $M' = 3$. The correction factors can be obtained based on the measurement on the lithium battery module. In this case, $a = 0.03714$, $b = 1.086$, $c = -0.1682$ and $d = 0.99$. Substituting these values into (13), the energy improvement efficiency curve can be derived.

Fig. 22 shows the comparison of the measured and modeled energy improvement efficiency under different power level with the idling time of 15 min. The different power level represents different discharge current of the battery modules. It is observed that the increased energy decreases slightly as the discharge current increases. The discharge current has limited influence on the effectiveness of the proposed control. The modeling results match the measured well. The maximum error between the measured and modeling results is about 7%. This is due to the nonlinear characteristic of the battery recovery effect. In addition, the analytical model does not take the loss of dc/dc converter into consideration.

2) Different Idling Time With the Same Power Level: In order to investigate the impact of different idling time on the effectiveness of the proposed self-reconfiguration control under the same power level, the idling time is set to be 5, 15 and 30 min, respectively. The power levels of 750 and 1500 W are used to make a sharp comparison. Figs. 23 and 24 show the discharge curve of the MBM under different discharge condition.

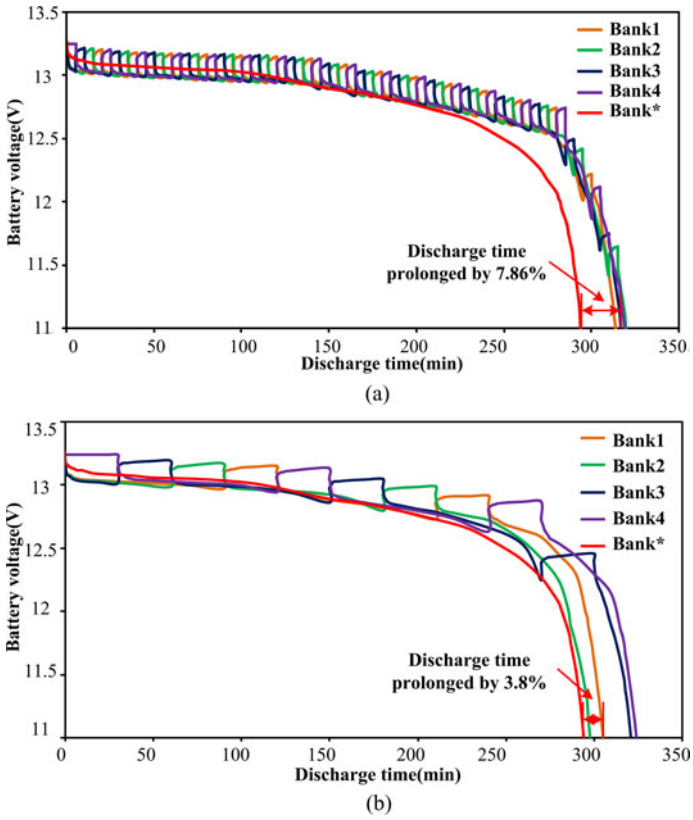

Fig. 23. Discharge curves with different idling time under the power level of 750 W. (a) 5 min; (b) 30 min.

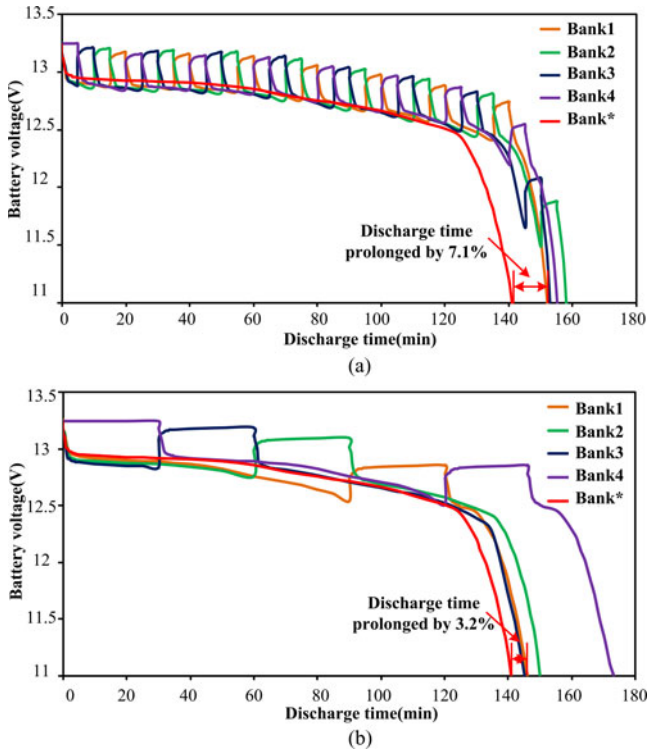

Fig. 24. Discharge curves with different idling time under the power level of 1500 W. (a) 5 min; (b) 30 min.

TABLE II
INCREASED ENERGY WITH DIFFERENT IDLING TIME

Power level	30 min	15 min	5 min
750 W	3.80%	6.12%	7.86%
1500 W	3.20%	5.67%	7.1%

Table II summarizes the measured energy improvement efficiency of the BESS under different discharge situation. It can be seen that the shorter idling time, higher efficiency can be achieved for both 750 and 1500 W.

Figs. 25 and 26 show the comparison of the measured and modeled energy improvement efficiency with different idling time under the power level of 750 and 1500 W, respectively. The maximum error between the measured and modeling results is around 8%. The measured and modeled results both show that the energy improvement efficiency decreases significantly as the idling time increases compared to Fig. 22. Therefore, a shorter idling time is preferred to realize the proposed control and improve the recovery energy efficiency. From Figs. 25 and 26, it is observed that the changing tendency of the energy improvement efficiency becomes gentle when the idling time reduces close to zero value. So, there is an optimal idling time for the proposed self-reconfiguration control theoretically. As a matter of fact, to further decrease the idling time is less effective as the energy improvement efficiency is limited. On the other hand, if the idling time is too small, it reduces the power conversion efficiency of the dc–dc converters during the reconfiguration progress and reduces the system stability.

As a conclusion, the effectiveness of the proposed control mainly depends on the idling time, and is nearly influenced by the discharge current. A shorter idling time is more favorable to realize the proposed control and there exists optimal idling time in the design. The proposed analytical model can predict the trend of the energy improvement efficiency versus the discharge current and idling time well and match the experimental results well.

B. Verification of Proposed VSF Control for the DAB Converter

In the part, the proposed VSF control for the DAB converter of the MBM is verified. Fig. 27 shows the control block diagram. In Fig. 27, the mode and f_s selection block are used to select the mode (CPM or TCM) and the switching frequency f_s based on the output power of the battery. M denotes the selected mode. For example, when the CPM is used, mode I will be enabled with the CPM. Otherwise, mode II will be enabled with the TCM. δ, f_s, D_1 and D_2 are used to generate the PWM register values in the DSP. D_1 and D_2 are

$$D_1 = 0.5,\ D_2 = 0.5 \qquad \text{(CPM)}$$
$$D_1 = \frac{2\delta}{\pi(1-k)},\ D_2 = \frac{2k\delta}{\pi(1-k)} \qquad \text{(TCM)}. \quad (15)$$

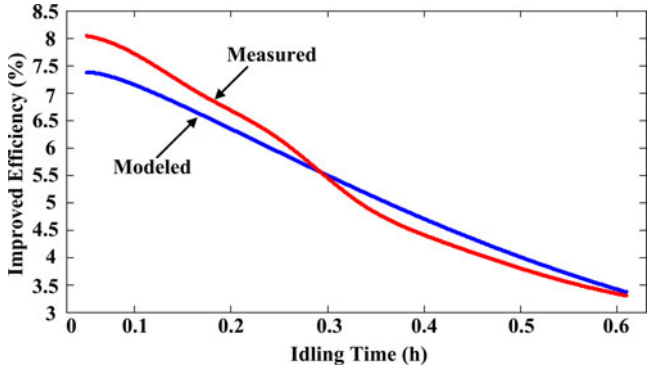

Fig. 25. Comparison of the measured and theoretical energy improvement efficiency with different idling time under the power level of 750 W.

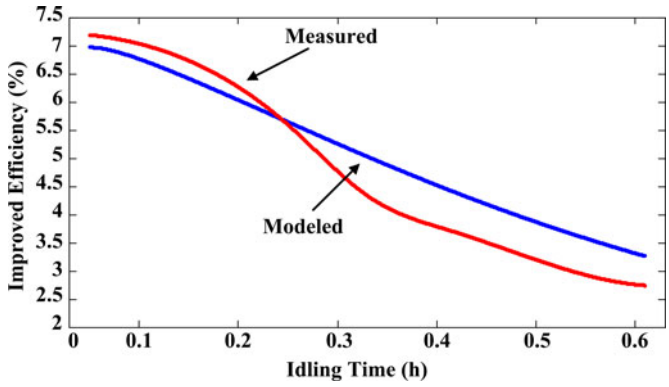

Fig. 26. Comparison of the measured and theoretical energy improvement efficiency with different idling time under the power level of 1500 W.

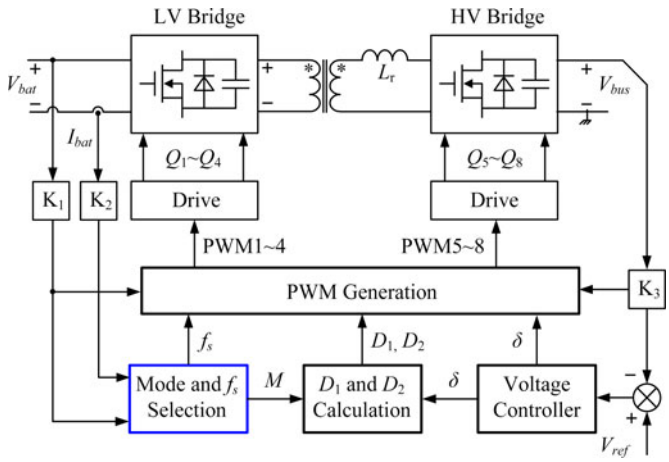

Fig. 27. Control diagram of the DAB converter.

Fig. 28 shows the key waveforms with different modulation strategies under 100-W load condition. As shown in Fig. 28(a), the peak current of the i_{Lr} is 4 A and the RMS current is high due to the continuous current with the conventional CPM. Fig. 28(b) shows the waveforms with the conventional TCM. Compared to Fig. 28(a), it is observed that lower peak (from 4 to 1.9 A) and RMS current can be achieved with the TCM (from 4 to 1.9 A), which results in the driving loss, the circulating loss and the switching loss reduction.

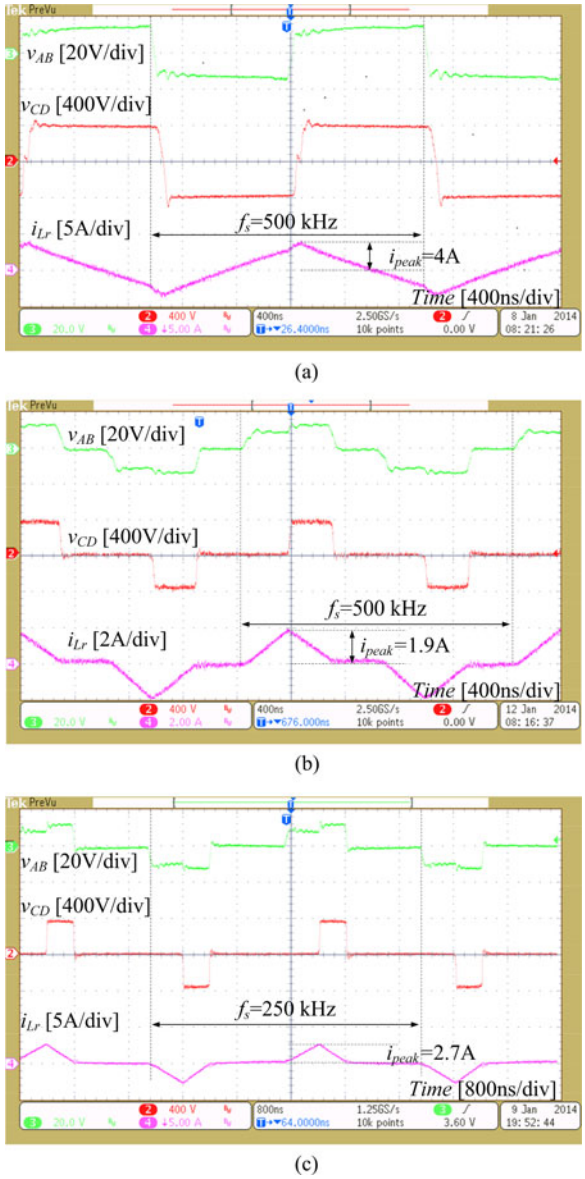

Fig. 28. Key waveforms with different modulation methods under 100-W load condition. (a) Conventional CPM: $f_s = 500$ kHz. (b) Conventional TCM: $f_s = 500$ kHz. (c) Proposed VSF hybrid TCM: $f_s = 250$ kHz.

Fig. 28(c) shows the key waveforms with the VSF hybrid TCM control under 100-W load condition. It is noted that the switching frequency is 250 kHz with the proposed control under 100-W load condition, which is half of the conventional CPM and TCM. The peak value of i_{Lr} is about $\sqrt{2}$ times of the TCM under 500 kHz (from 1.9 to 2.7 A), but still lower than the CPM under 500 kHz. The proposed VSF TCM minimizes the dominant loss which helps to achieve high efficiency since the frequency related loss (the drive loss and switching loss) is dominant under 100-W load condition.

Fig. 29 shows the measured efficiency comparison between the CPM, the CSF hybrid control and the proposed VSF

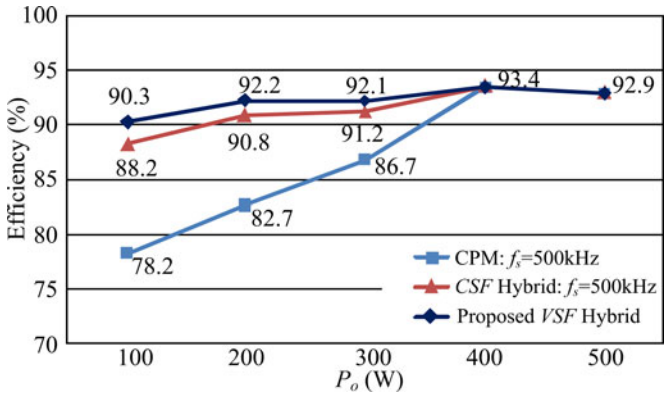

Fig. 29. Efficiency comparison; top: proposed VSF hybrid control; mid: CSF hybrid control: $f_s = 500$ kHz; bottom: conventional CPM: $f_s = 500$ kHz.

hybrid control. It is observed that under light load condition of 100 W, the efficiency is improved from 78.2% to 88.2% (an improvement of 10.0%) with the CSF hybrid control. With the proposed VSF hybrid control, the efficiency is further improved from 88.2% to 90.3% (an improvement of 2.1%) since the VSF TCM is more effective to reduce the dominant loss. Differently from the conventional approaches previously proposed, the VSF hybrid control in this paper is based on the overall loss optimization method directly other than reduction of the reactive power or RMS current.

VII. Conclusion

To overcome drawbacks of the centralized BESS, a new distributed architecture of BESS based on the MBMs is proposed in this paper. The MBM consists of a microbidirectional dc/dc converter, a micro-BMS and a cell bank. Moreover, a self-reconfiguration control strategy based on the battery recovery effect is proposed to further improve the energy efficiency in the distributed BESS. An efficiency analytical model considering the recovery effect is proposed using the curve fitting method. The DAB converters are chosen as the microbidirectional dc/dc converters and a hybrid VSF control is proposed to achieve high efficiency in wide load range.

An experimental testing platform of 1.5 kW consisting of four MBMs and four 12 V/100 Ah lithium battery modules was built to verify the proposed architecture and control. The experimental results verified the effectiveness of the proposed control strategy. With the idling time of 15 min, the discharge efficiency is improved by 5.67% under the power level of 1500 W. Similarly, the discharge efficiency is improved by 7.1% and 3.2% under different idling time of 5 and 30 min with the power level of 1500 W, respectively. The effectiveness of the proposed self-reconfiguration control mainly depends on the idling time, and is nearly influenced by the discharge current. A shorter idling time is more favorable to realize the proposed self-reconfiguration control and there exists optimal idling time in the design. The efficiency analytical model considering the recovery effect of the batteries is verified by the experimental results. This model can be used to predict the trend of the energy improvement efficiency versus the discharge current and idling time well. The 12 V/380 V/500 W DAB converters with the switching frequency range from 250 to 500 kHz were built to function as MBMs. An efficiency improvement of 2.1% is achieved with the proposed VSF hybrid control under 20% load condition.

Acknowledgment

The authors would like to thank for the experimental facilities supported by LITE-ON RESEARCH PROGRAM and the Priority Academic Program Development of Jiangsu Higher Education Institutions.

References

[1] R. H. Lasseter, "Microgrid: A conceptual solution," in *Proc. IEEE Power Electron. Spec. Conf.*, 2004, pp. 4285–4290.
[2] S. Luo and I. Batarseh, "A review of distributed power systems," *IEEE Aerosp. Electron. Syst. Mag.*, vol. 20, no. 8, pp. 5–16, Aug. 2005.
[3] K. Strunz, E. Abbasi, and D. N. Huu, "DC microgrid for wind and solar power integration," *J. Emerging Sel. Topics Power Electron.*, vol. 2, no. 1, pp. 115–126, Mar. 2014.
[4] W. Zhang, D. Dong, I. Cvetkovic, F. C. Lee, and D. Boroyevich, "Lithium-based energy storage management for DC distributed renewable energy system," in *Proc. IEEE Energy Convers. Congr. Expo.*, 2011, pp. 3270–3277.
[5] D. Boroyevich, I. Cvetkovic, R. Burgos, and D. Dong, "Intergrid: A future electronic energy network?," *J. Emerging Sel. Topics Power Electron.*, vol. 1, no. 3, pp. 127–138, Sep. 2013.
[6] L. Roggia, L. Schuch, J. E. Baggio, C. Rech, and J. R. Pinheiro, "Integrated full-bridge-forward DC–DC converter for a residential microgrid application," *IEEE Trans. Power Electron.*, vol. 28, no. 4, pp. 1728–1740, Apr. 2013.
[7] B. Zhao, Q. Song, W. Liu, and Y. Sun, "Overview of dual-active-bridge isolated bidirectional DC-DC converter for high-frequency-link power-conversion system," *IEEE Trans. Power Electron.*, vol. 29, no. 8, pp. 4091–4106, Aug. 2014.
[8] Z. Ye, "Dual half-bridge DC–DC converter with wide-range ZVS and zero circulating current," *IEEE Trans. Power Electron.*, vol. 28, no. 7, pp. 3276–3286, Jul. 2013.
[9] A. Aboushady, K. H. Ahmed, S. J. Finney, and B. W. Williams, "Linearized large signal modeling, analysis, and control design of phase-controlled series-parallel resonant converters using state feedback," *IEEE Trans. Power Electron.*, vol. 28, no. 8, pp. 3896–3911, Aug. 2013.
[10] N. M. L. Tan, T. Abe, and H. Akagi, "Design and performance of a bidirectional isolated dc-dc converter for a battery energy storage system," *IEEE Trans. Power Electron.*, vol. 27, no. 3, pp. 1237–1248, Mar. 2012.
[11] J. Kan, S. Xie, Y. Tang, and Y. Wu, "Voltage-fed dual active bridge bidirectional DC/DC converter with an immittance network," *IEEE Trans. Power Electron.*, vol. 29, no. 7, pp. 3582–3590, Jul. 2014.
[12] X. Li and Y. F. Li, "An optimized phase-shift modulation for fast transient response in a dual-active-bridge converter," *IEEE Trans. Power Electron.*, vol. 29, no. 6, pp. 2661–2665, Jun. 2014.
[13] A. K. Jain and R. Ayyanar, "PWM control of dual active bridge: Comprehensive analysis and experimental verification," *IEEE Trans. Power Electron.*, vol. 26, no. 4, pp. 1215–1227, Apr. 2011.
[14] B. Zhao, Q. Yu, and W. Sun, " Extended-phase-shift control of isolated bidirectional DC-DC converter for power distribution in microgrid," *IEEE Trans. Power Electron.*, vol. 27, no. 11, pp. 4667–4680, Nov. 2012.
[15] B. Zhao, Q. Song, and W. Liu, "Efficiency characterization and optimization of isolated bidirectional DC-DC converter based on dual-phase-shift control for DC distribution application," *IEEE Trans. Power Electron.*, vol. 28, no. 4, pp. 1711–1727, Apr. 2013.
[16] F. Krismer and J. W. Kolar, "Closed form solution for minimum conduction loss modulation of DAB converters," *IEEE Trans. Power Electron.*, vol. 27, no. 1, pp. 174–188, Jan. 2012.
[17] C. Chau, F. Qin, S. Sayed, and Y. Yang, "Harnessing battery recovery effect in wireless sensor networks experiments and analysis," *IEEE J. Sel. Areas Commun.*, vol. 28, no. 7, pp. 1222–1232, Sep. 2010.
[18] C. Chau, F. Qin, S. Sayed, and Y. Yang, "Battery recovery aware sensor networks," in *Proc. Int. Conf. Modeling Optimization Mobile*, Jun. 2009, pp. 1–9.

[19] V. Rao, G. Singhal, A. Kumar, and N. Navet, "Battery model for embedded systems," in *Proc. Int. Conf. VLSI Design*, Jan. 2005, pp. 105–110.
[20] T. Kim, W. Qiao, and L. Qu, "A series-connected self-reconfigurable multicell battery capable of safe and effective charging/ discharging and balancing operations," in *Proc. IEEE Appl. Power Electron. Conf. Expo.*, 2012, pp. 2259–2264.
[21] S. Ci, J. Zhang, H. Sharif, and M. Alahmad, "Dynamic reconfigurable multi-cell battery: A novel approach to improve battery performance," in *Proc. IEEE Appl. Power Electron. Conf. Expo.*, 2012, pp. 439–442.
[22] L. Song and J. W. Evans, "Electrochemical-thermal model of lithium polymer batteries," *J. Electrochem. Soc.*, vol. 147, pp. 2086–2095, 2000.
[23] D. W. Dennis, V. S. Battaglia, and A. Belanger, "Electrochemical modeling of lithium polymer batteries," *J. Power Sources*, vol. 110, no. 2, pp. 310–320, Aug. 2002.
[24] J. Newman, K. E. Thomas, H. Hafezi, and D. R. Wheeler, "Modeling of lithium-ion batteries," *J. Power Sources*, vol. 119–121, pp. 838–843, Jun. 2003.
[25] C. Kroeze and T. Krein, "Electrical battery model for use in dynamic electric vehicle simulations," in *Proc. IEEE Power Electron. Spec. Conf.*, 2008, pp. 1336–1342.
[26] S. Buller, M. Thele, R. W. D. Doncker, and E. Karden, "Impedance based simulation models of supercapacitors and Li-ion batteries for power electronic applications," in *Proc. Conf. Rec. Ind. Appl. Conf.*, 2003, pp. 1596–1600.
[27] M. Chen and G. A. Rincon-Mora, "Accurate electrical battery model capable of predicting runtime and I-V performance," *IEEE Trans. Energy Convers.*, vol. 21, no. 2, pp. 504–511, Jun. 2006.
[28] L. Gao, S. Liu, and A. Dougal, "Dynamic lithium-ion battery model for system simulation," *IEEE Trans. Compon. Packag. Technol.*, vol. 25, no. 3, pp. 495–505, Sep. 2002.
[29] T. Kim and W. Qiao, "A hybrid battery model capable of capturing dynamic circuit characteristics and nonlinear capacity effects," *IEEE Trans. Energy Convers.*, vol. 26, no. 4, pp. 1172–1180, Dec. 2011.
[30] N. EI Agroudi and Y. Ismail, "New hybrid battery model that takes into account both electric circuit characteristics and non-linear battery properties," in *Proc. IEEE Int. Conf. Electron., Circuits Syst.*, 2013, pp. 289–292.

Zhiliang Zhang (S'03–M'09–SM'14) received the B.Sc. and M.Sc. degrees in electrical and automation engineering from the Nanjing University of Aeronautics and Astronautics (NUAA), Nanjing, China, in 2002 and 2005, respectively, and the Ph.D. degree from the Department of Electrical and Computer Engineering, Queen's University, Kingston, ON, Canada, in 2009.

In June 2009, he joined NUAA and he is currently a Professor with Aero-Power Sci-Tech Center. His research interests include high-frequency power converters and renewable energy power conversion system. He worked as a Design Engineering Intern from June 2007 to September 2007, at Burlington Design Center, VT, Linear Technology Corporation. He was a Winner of "United Technologies Corporation Rong Hong Endowment" in 1999. He serves as Secretary of PELS Technical Committee on Power and Control Core Technologies since 2013.

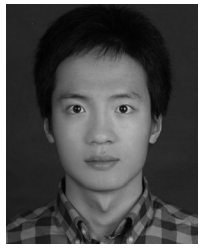

Yong-Yong Cai (S'13) received the B.S. degree in electrical engineering from the Nanjing University of Aeronautics and Astronautics (NUAA), Nanjing, China, in 2012. He is currently working toward the M.S. degree at the Aero-Power Sci-Tech Center, NUAA.

His research interests include battery management systems and bidirectional dc–dc converters.

Yue Zhang received the B.S. degree in electrical engineering from the Nanjing University of Aeronautics and Astronautics (NUAA), Nanjing, China, in 2012. He is currently working toward the M.S. degree at the Aero-Power Sci-Tech Center, NUAA.

His research interests include the photovoltaic microinverters and converters for the battery energy storage system.

Dong-Jie Gu received the B.S. degree in electrical engineering from the Nanjing University of Aeronautics and Astronautics (NUAA), Nanjing, China, in 2014, where he is currently working toward the M.S. degree at the Aero-Power Sci-Tech Center, NUAA.

His research interest includes battery management system for power electronics system.

Yan-Fei Liu (M'94–SM'97–F'13) received the Ph.D. degree from the Department of Electrical and Computer Engineering, Queen's University, Kingston, ON, Canada, in 1994.

From February 1994 to July 1999, he worked as a Technical Advisor with the Advanced Power System Division, Nortel Networks. Since 1999, he joined Queen's University. He is currently a Professor at the Department of Electrical and Computer Engineering. His research interests include digital control technologies for high efficiency, fast dynamic response dc–dc switching converter and ac–dc converter with power factor correction, resonant converters and server power supplies, and LED drivers. He holds 22 US patents and has published more than 130 technical papers in IEEE transactions and conferences. He is also a principal contributor for two IEEE standards.

Dr. Liu serves as an Editor of the IEEE JOURNAL OF EMERGING AND SELECTED TOPICS OF POWER ELECTRONICS since 2012, an Associate Editor for the IEEE TRANSACTIONS ON POWER ELECTRONICS since 2001, an Editor-in-Chief for Special Issue of Power Supply on Chip of the IEEE TRANSACTIONS ON POWER ELECTRONICS from 2011 to 2013, as well as the Technical Program Cochair for ECCE 2011. He serves as the Chair of PELS Technical Committee on Control and Modeling Core Technologies since 2013. He served as the Chair of PELS Technical Committee on Power Conversion Systems and Components from 2009 to 2012.